ANTIOXIDANTS & REDOX SIGNALING
Volume 28, Number 15, 2018

DOI: 10.1089/ars.2017.7329

Discoveries

FORUM REVIEW ARTICLE

In Vivo Molecular Electron Paramagnetic Resonance-Based Spectroscopy and Imaging of Tumor Microenvironment and Redox Using Functional Paramagnetic Probes

Valery V. Khramtsov[1,2]

Abstract

Significance: A key role of the tumor microenvironment (TME) in cancer progression, treatment resistance, and as a target for therapeutic intervention is increasingly appreciated. Among important physiological components of the TME are tissue hypoxia, acidosis, high reducing capacity, elevated concentrations of intracellular glutathione (GSH), and interstitial inorganic phosphate (Pi). Noninvasive *in vivo* pO_2, pH, GSH, Pi, and redox assessment provide unique insights into biological processes in the TME, and may serve as a tool for preclinical screening of anticancer drugs and optimizing TME-targeted therapeutic strategies.
Recent Advances: A reasonable radiofrequency penetration depth in living tissues and progress in development of functional paramagnetic probes make low-field electron paramagnetic resonance (EPR)-based spectroscopy and imaging the most appropriate approaches for noninvasive assessment of the TME parameters.
Critical Issues: Here we overview the current status of EPR approaches used in combination with functional paramagnetic probes that provide quantitative information on chemical TME and redox (pO_2, pH, redox status, Pi, and GSH). In particular, an application of a recently developed dual-function pH and redox nitroxide probe and multifunctional trityl probe provides unsurpassed opportunity for *in vivo* concurrent measurements of several TME parameters in preclinical studies. The measurements of several parameters using a single probe allow for their correlation analyses independent of probe distribution and time of measurements.
Future Directions: The recent progress in clinical EPR instrumentation and development of biocompatible paramagnetic probes for *in vivo* multifunctional TME profiling eventually will make possible translation of these EPR techniques into clinical settings to improve prediction power of early diagnostics for the malignant transition and for future rational design of TME-targeted anticancer therapeutics. *Antioxid. Redox Signal*. 28, 1365–1377.

Keywords: tumor microenvironment, electron paramagnetic resonance, tumor hypoxia, tumor acidosis, tumor redox, paramagnetic probes

Introduction

TUMOR MICROENVIRONMENT (TME) is a key support system of cancer that includes physical components such as extracellular matrix, blood vessels, and various types of cells of the particular organ, and physiological components. Among TME parameters of critical importance for physiology in solid tumors, compromised tissue oxygenation (101, 104), acidification (12, 37), accumulation of reducing equivalents (81), elevated concentrations of intracellular glutathione (GSH) (33, 105), and interstitial inorganic phosphate (Pi) (9) are well documented. Tumor tissue hypoxia (101) resulted from the undeveloped blood vessels is associated with a higher dependence on glycolytic metabolism (106) and corresponding TME acidosis (12, 37, 44). Metabolic alterations affect the tissue redox and result in accumulation of reducing equivalents (81), including a significant increase of GSH, key component of intracellular redox buffer (33, 105). Interstitial Pi has been

[1]*In Vivo* Multifunctional Magnetic Resonance center, Robert C. Byrd Health Sciences Center, West Virginia University, Morgantown, West Virginia.
[2]Department of Biochemistry, West Virginia University School of Medicine, Morgantown, West Virginia.

recently recognized as an emerging signaling molecule playing a role in promoting cell transformation and tumorigenesis (14–16, 51, 52, 97), and a new TME marker of tumor progression and aggressiveness (9).

Individual cancer cells generated by causal genetic insults behave differently depending on their specific tissue microenvironment. Numerous therapeutic strategies elaborated in cellular systems *in vitro* in the absence of TME factors are not reproduced in further studies in animals and humans. There is approaching scientific consensus that *in vivo* TME profiling opens opportunities for preclinical screening of anticancer drugs and predicting therapeutic effectiveness, as well as developing new diagnostics and noninvasive guided therapeutic strategies based on TME manipulation.

A reasonable radiofrequency penetration depth in tissues makes magnetic resonance imaging (MRI) and low-field electron paramagnetic resonance (EPR)-based techniques the most appropriate approaches for noninvasive assessment of the chemical TME parameters such as pO_2, extracellular pH (pH_e), phosphate (Pi), GSH, and redox. MRI relies largely on imaging of water protons and is widely used in clinical settings providing anatomical resolution while lacking functional sensitivity. Potentially attractive ^{31}P NMR measurements of extracellular [Pi] and pH based on a signal from endogenous phosphate are normally masked by several-fold higher intracellular Pi concentrations (36, 37). In contrary to the NMR applications, EPR measurements rely on spectroscopy and imaging of specially designed paramagnetic probes providing functional sensitivity. Note that exogenous EPR probes have advantages over exogenous NMR probes due to a much higher intrinsic sensitivity of EPR and absence of endogenous background EPR signals.

In vivo EPR applications rely on use of both particulate and soluble paramagnetic probes (see Fig. 1 for the exemplified structures). Advantages of particulate probes used for EPR oximetry are high functional sensitivity, stability in living tissue, and minimal toxicity (11, 34, 76, 90). The particulate probe may remain in the place of implantation for long periods of time, enabling repeated measurements of tissue pO_2 for up to weeks and months after implantation. On the contrary, soluble nitroxide (NR) and triarylmethyl (TAM) probes may possess functional sensitivity to various parameters of TME such as pO_2, pH, Pi, redox, and GSH (9, 10, 20, 93) and allow for spatially resolved measurements using EPR-based imaging techniques (13, 29, 66, 70, 94). The developments of a dual-function pH and redox nitroxide probes, NR1 and NR2 (10, 94), GSH probe (59, 93), and multifunctional pH, pO_2, and Pi trityl probe (20), shown in Figure 2, provide unsurpassed opportunities for *in vivo* concurrent measurements of several TME parameters and their correlation analyses independent of probe distribution and time of measurement (9). Here we overview the recent advances of *in vivo* molecular EPR-based spectroscopy and imaging of TME and redox using functional paramagnetic probes, and applications of these approaches in various animal models of cancer.

In vivo *EPR oximetry of TME*

Significant oxygen deficiency has been reported for many tumors, which is associated with the tumor-increased resistance toward radiation and chemotherapy (19, 47, 104). The hypoxic TME promotes processes driving malignant progression, such as angiogenesis, genetic instability, and metastasis (46, 83). Therefore, noninvasive and real-time pO_2 measurements using EPR oximetry are of importance in preclinical research and have the potential for clinical applications (100).

EPR oximetry is predominantly based on the physical phenomenon of Heisenberg spin exchange between the molecules of paramagnetic probe and oxygen, which does not interfere with oxygen metabolism, therefore providing basis for noninvasive EPR oxygen measurements in biological systems. Spin-exchange of the radical probe with comparatively long relaxation time and oxygen diradical molecule with short relaxation time results in shortening both the longitudinal (T_1) and transverse (T_2) relaxation times of the probe in inverse proportionality to the rate of encounter of probe and oxygen molecules, which in turn is proportional to oxygen concentration and oxygen partial pressure (27, 49). NRs were the first paramagnetic probes used for EPR oximetry (2, 3, 41, 71). Backer *et al.* (3) pioneered applications of continuous waves (CW) EPR T_2 oximetry method based

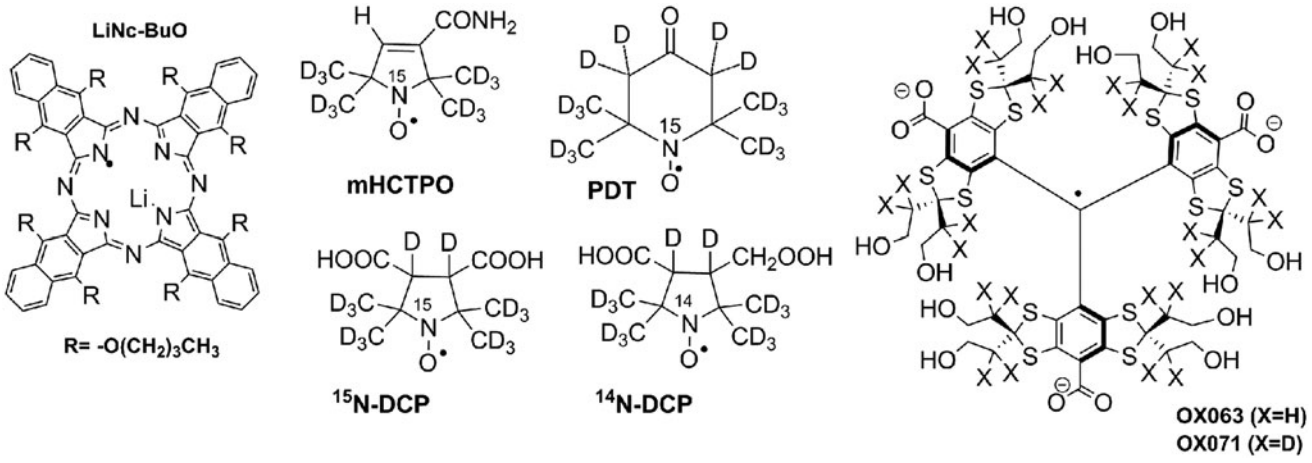

FIG. 1. Chemical structures of the EPR oximetric probes discussed in the text. Particulate LiNc-BuO, soluble nitroxide probes, mHCTPO, PDT, ^{15}N-DCP, and ^{14}N-DCP, and soluble trityl radicals, OX063 and OX071. EPR, electron paramagnetic resonance.

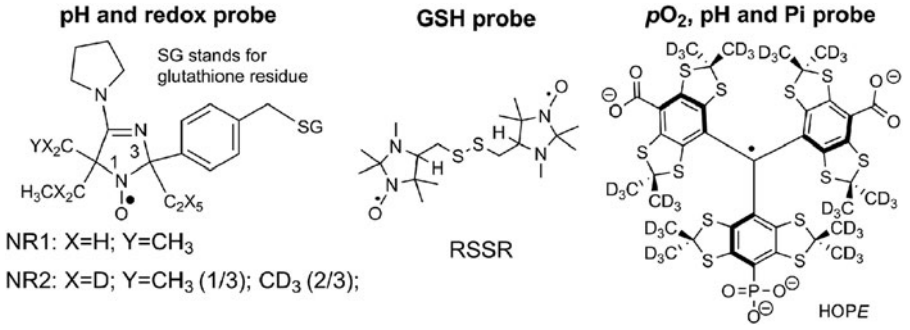

FIG. 2. Chemical structures of the soluble paramagnetic probes for multifunctional TME profiling discussed in the text. pH and redox probes, NR1 and its deuterated analog, NR2; disulfide biradical probe for GSH detection, RSSR; and multifunctional pH, pO_2, and Pi probe of *extracellular* microenvironment, HOP*E*. GSH, glutathione; TME, tumor microenvironment.

on oxygen-induced line broadening of the NR probe (for Lorentzian lineshape EPR linewidth, $\Delta H = 1/(\gamma_e T_2)$, where $\gamma_e = 1.76 \times 10^7$ s^{-1} Gauss^{-1} is electron gyromagnetic ratio). In this approach, accuracy of pO_2 measurements is largely defined by the probe linewidth and oxygen-induced line broadening effect. For aqueous NR solutions, the typical value of the line-broadening effect is about 500 mG/m*M* of oxygen ($\approx$0.6 mG/mmHg of pO_2), which results in comparatively low accuracy of pO_2 measurements using the NR probes with a typical linewidth of about 1 G (ca. ±20 mmHg of pO_2). The use of perdeuterated NRs (such as PDT, Fig. 1) significantly increases accuracy of pO_2 assessment (68) but still the measurements are complicated by overlap of the effects of oxygen-induced line broadening and concentration-induced line broadening (ca. 100–200 mG/m*M*). To discriminate between the latter two factors, Halpern *et al.* (41) used partially deuterated mHCTPO NR (Fig. 1) with only one observable superhyperfine splitting originated from hydrogen atom at carbon C4 of heterocycle. Both oxygen and radical concentrations affect the linewidth, while only an increase in probe concentration but not oxygen results in narrowing of hydrogen hyperfine splitting. Authors demonstrated method utility for noninvasive assessment of TME oxygenation, for example, observing a clear pO_2 difference measured in a mouse model of FSa tumor for animals breathing oxygen (42 ± 8 mmHg) or air (7 ± 8 mmHg). Recently, an alternative approach to discriminate between oxygen- and concentration-induced line broadenings of the NR probes has been proposed by Kubota *et al.* (67) based on the use of two isotopic forms of perdeuterated dicarboxy pyrrolidine NR (Fig. 1). ^{15}N-DCP and ^{14}N-DCP NRs show the different concentration-induced line broadenings, in part, due to the different nuclear statistical factors equal to 1/2 and 2/3 correspondingly, the consequence of absence of line broadening for the spin-exchange between the NRs with the same projections of nitrogen nuclear spin (86).

The NRs were the first probes explored for mapping oxygen environment using EPR imaging (EPRI) (68) and dynamic nuclear polarization imaging (40) (also termed proton/electron double-resonance imaging, PEDRI, or Overhauser-enhanced MRI, OMRI). However, comparatively broad NR spectral lines complicate their oximetric imaging application, particularly for pulsed EPRI (50). Further progress in EPR oximetry was enabled by the development of the trityl radicals or TAMs by Nycomed Innovation (1). TAM probes show a single narrow EPR line with the width of about 100 mG or lower [160 mG for OX063 and 80 mG for OX071 (27), see Fig. 1 for the structures]. The oxygen-induced line broadening of the TAMs in aqueous solutions is about 500 mG/m*M* of oxygen (1, 6), similar to that for the NRs, while the concentration broadening is about 10 mG/m*M* (1, 82), which is one order of magnitude less than that for the NRs. These factors make TAMs preferable EPR oximetric soluble probes with oxygen sensitivity approaching 1 mmHg of pO_2.

TAM probes were first proposed as advanced oximetric probes for PEDRI (66) due to their long relaxation times allowing for easy saturation of EPR transitions. The presence of oxygen shortens the relaxation times and consequently results in the decreased transfer of polarization from electron to nuclear spins during the EPR irradiation. *In vivo* oximetry is one of the most straightforward and useful applications of PEDRI (1, 66) overviewed by Kishimoto *et al.* in a separate review of this Forum (61).

Elas *et al.* (23) demonstrated a utility of CW EPRI using TAM probes for pO_2 mapping and identifying hypoxic areas in TME. Spectral–spatial CW EPRI provided spatial resolution of (1 mm)^3 and pO_2 accuracy of about 3–4 mmHg with acquisition time of about 20 min (23). Long relaxation times of the TAM probes open opportunity to apply pulsed EPR techniques further advancing pO_2 mapping. In addition to elimination of object motion artifacts, pulsed EPRI decreases acquisition times. Time-domain pulsed EPR measurements of free induction decay allow for imaging the decay time, (T_2^*), or linewidth, ($\Delta H = 1/(\gamma_e T_2^*)$, converted to pO_2 map (82). Applications of pulsed EPR oximetry to image TME, including monitoring kinetics of tumor oxygenation, validation of hypoxic cancer models, coregistration with other imaging modalities, and treatment response to anticancer therapy, are overviewed in a separate review of this Forum (62). Note that accuracy of oxygen measurements using T_2^*-based Fourier transform EPRI can be affected by concentration-induced line broadening, for example, at high local probe concentrations often used in imaging experiments.

Recently, Halpern and colleagues (27, 28, 30) demonstrated that spin-lattice relaxation (T_1)-based EPRI oximetry using TAM probes has significant advantages compared to (T_2)-based analogs. Both longitudinal and transverse relaxation rates, R1 and R2, or the corresponding inverse relaxation times, $1/T_1$ and $1/T_2$, of TAMs are linearly proportional to pO_2 with a similar sensitivity. However, T_1 is about one order of magnitude less sensitive to probe concentration self-relaxation compared with that for T_2. This facilitates high-precision measurements and imaging of the oxygen tension using spin-lattice relaxation EPR in live animal tissues with 1 mmHg pO_2 resolution and 1 mm spatial resolution, and

acquisition time of 10 min or less. An exemplified three-dimensional oxygen map of fibrosarcoma tumor obtained with T_1-based EPRI is shown in Figure 3 demonstrating high pO_2 heterogeneity of TME and clearly identifying hypoxic areas (29).

Authors suggested (29) that that EPR images of tumor regions with low oxygenation can be used as a tool to guide radiation therapy. The first preliminary data obtained in a fibrosarcoma mouse model with targeting small hypoxic areas of tumor using conformal radiation therapy demonstrate the promising enhancement of cancer radiation treatment. Current development of the EPR imaging oximetry using TAM probes such asOX071 (29) opens the path to human applications but their potential clinical translation hinges on achieving regulatory approval for the use of these imaging agents in human subjects, requiring significant investment.

Particulate probes have certain advantages for potential clinical translation. In addition to already mentioned high functional sensitivity, stability in living tissue, minimal toxicity, and capacity for repetitive measurements during months after implantation (11, 34, 76, 90, 99, 100, 107), they can more readily be approved for use in human subjects. Of the particulate oximetric probes, India ink has been previously approved for clinical use as an anatomical marker, and it has been the first probe used for tissue pO_2 measurements in humans by Swartz and his colleagues (99, 107). Alternative probes such as LiPc derivatives (76, 89, 91) have an advantage over India ink in oxygen sensitivity. Recently, Kuppusamy and his colleagues encapsulated LiNc-BuO probe (Fig. 1) in an oxygen-permeable polymer polydimethylsiloxane (84, 85), a biocompatible silicone material used in a wide range of medical applications. The authors termed the obtained oxygen sensor as OxyChip and demonstrated its high oxygen sensitivity and safety in animal models (84, 85). Recently, the Phase I clinical trial on oxygen measurements in subcutaneous tumors by EPR oximetry using OxyChip has been sponsored by the Dartmouth-Hitchcock Medical Center and National Cancer Institute (17).

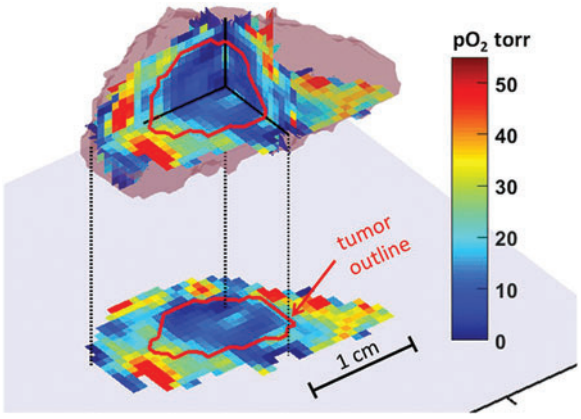

FIG. 3. Three-dimensional oxygen map of mouse fibrosarcoma tumor bearing leg. Tumor outline, from a registered MRI image, is shown in *red*. Reproduced from Ref. (29) with permission. MRI, magnetic resonance imaging. To see this illustration in color, the reader is referred to the web version of this article at www.liebertpub.com/ars

In vivo *EPR assessment of reducing capacity and acidosis of TME*

Tumor reliance on glycolysis is known to generate significant alterations in the TME acidity and redox status. Areas of hypoxia and acidosis are common features of TME in solid tumors. Cells that exist in such adverse TME conditions can significantly alter the tumor response to cytotoxic anticancer therapies. The acidic extracellular pH in tumors has a number of important consequences, playing a role in tumor initiation, progression, and therapy (37). pH_e has been identified as a significant prognostic factor both in experimental transplantable tumor models and in spontaneous tumors (79). In its turn, high reducing capacity of TME is an important determinant in the response of the tumor to certain chemotherapeutic agents, radiation, and bioreductive cell cytotoxins (18).

NRs and TAMs containing ionizable group with an equilibrium constant K_a, exist in aqueous solution in protonated, RH^+, and unprotonated, R, forms. EPR measurements of the ratio of their concentrations allow for calculation of the pH values based on the Henderson–Hasselbalch equation, $[RH^+]/[R] = [H^+]/K_a$. Among the various NR types, imidazoline and imidazolidine nitroxides have been used in most EPR spectroscopy and imaging pH metric applications (53, 56) due to the significant changes of the EPR spectral parameters on protonation of nitrogen atom N-3 ($\Delta a_N \approx 1$ G and $\Delta g \approx 0.0002$) (58). Recently, pH-sensitive trityl radicals were also synthesized (7, 20). One of the great strengths of the EPR pH probes is that the method is ratiometric, the pH measurement being independent of the probe concentration but dependent on the ratio, $[RH^+]/[R]$. Spectral simulation or spectral parameters sensitive to $[RH^+]/[R]$ ratio can be used for accurate pH determination. The spectral parameters used as pH markers include the ratio of peak intensities when RH^+

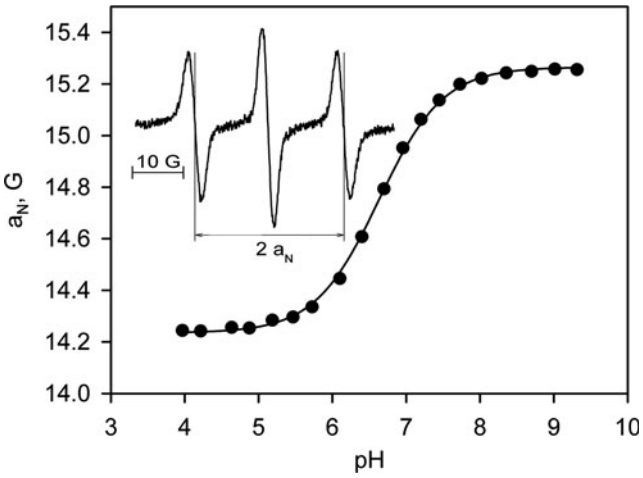

FIG. 4. pH-Dependence of the observed hyperfine splitting constant, a_N, of the NR1 probe. L-band EPR spectra were acquired at 37°C. The *solid line* is the fit of experimental data with standard titration *curve* $a_N = (a_N(NR1 - H^+) + a_N(NR1)\ 10^{pH-pK})/(1 + 10^{pH-pK})$ yielding $pK_a = 6.6$, $a_N(NR1\text{-}H^+) = 14.24$ G, and $a_N(NR1) = 15.27$ G. *Insert*: Exemplified EPR spectrum of 1 m*M* NR1 solution. The measured hyperfine splitting constant, 14.63 G. Adapted from Ref. (64) with permission from John Wiley & Sons, Inc.

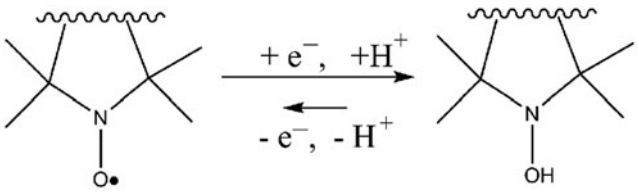

FIG. 5. Illustration of the nitroxide/hydroxylamine redox couple. In living tissue, one-electron reduction of the nitroxides prevails over hydroxylamine oxidation and the equilibrium is strongly shifted toward the hydroxylamine (63).

and R signals are resolved, and the observed hyperfine splitting, a_N, measured as a distance between the EPR lines of the triplet when RH^+ and R signals are overlapped. Sensitivity of the observed a_N value to pH depends on the spectrometer frequency and settings such as modulation amplitude (57).

Figure 4 shows the observed a_N dependence of the NR1 radical on pH described by a standard titration curve. Note that the structure of NR1 probe has been specially designed for the pH measurements in extracellular TME. First, value of the pK_a of the NR1 radical, 6.6 at 37°C (10), allows for *in vivo* pH measurements in the range from 5.6 to 7.6 (accuracy, 0.05 pH units), which covers the range of acidic pH in solid tumors. Binding of cell-impermeable GSH tripeptide to the NR1 restricts its penetration into the cells ensuring EPR measurements of extracellular pH values (108). The bulky ethyl groups at carbons C2 and C5 provide steric hindrance around the radical fragment significantly decreasing the rate of reduction (60) in a highly reducing microenvironment.

The EPR signal decay due to NR reduction to the corresponding hydroxylamines (Fig. 5) in living tissues is often considered as a limiting factor in EPR applications of the NR probes. On the positive side, the rates of the nitroxide decay allow for EPR evaluation of the tissue reducing capacity in various physiological and pathophysiological states (10, 70, 88). In its turn, cyclic hydroxylamines can be oxidized by biological oxidants into the corresponding EPR-measured NRs and provide useful information on oxidative stress and reactive oxygen species (ROS) generation. In contrast to the EPR spin-trapping approach (4, 43), oxidation of hydroxylamines is not oxidant specific and their use to measure specific ROS requires additional controls. *In vitro* and *in vivo* applications of cyclic hydroxylamine are reviewed in this Forum by Dikalov *et al.* (21).

An application of cell-permeable NRs allows for EPR assessment of intracellular redox status (69, 70), while application of cell-impermeable NRs allows for assessment of the reducing capacity of extracellular matrix. Note that in case of pH-sensitive NRs, redox-sensitive marker, signal amplitude, and pH-sensitive marker, a_N, are independent spectral parameters, therefore making these NRs dual-function pH and redox probes. Figure 6 exemplifies the pH and redox measurements in mouse model of breast cancer (10) using NR1 probe. The data obtained for the group of female FVB/N MMTV-PyMT mice in tumors and normal mammary glands support extracellular acidosis and high reducing capacity of TME.

Note that tumor tissue is characterized by high heterogeneity, and therefore, spatially resolved functional measurements of TME are critically important, for example, allowing identification of the area with compromised redox and pH homeostasis. Both EPR imaging (13, 54, 70) and PEDRI (65, 94) were explored for redox and pH mapping. In case of PEDRI, the deuterated analog of the NR1 probe, NR2 (Fig. 2), has been used for pH mapping of TME in mouse model of breast cancer (61, 94). The narrow signal of the deuterated NR2 probe is easily saturated by EPR irradiation, which results in high PEDRI signal enhancement and allows for shorter acquisition time. PEDRI applications for pH and redox mapping of TME are discussed in a separate article of this Forum (61).

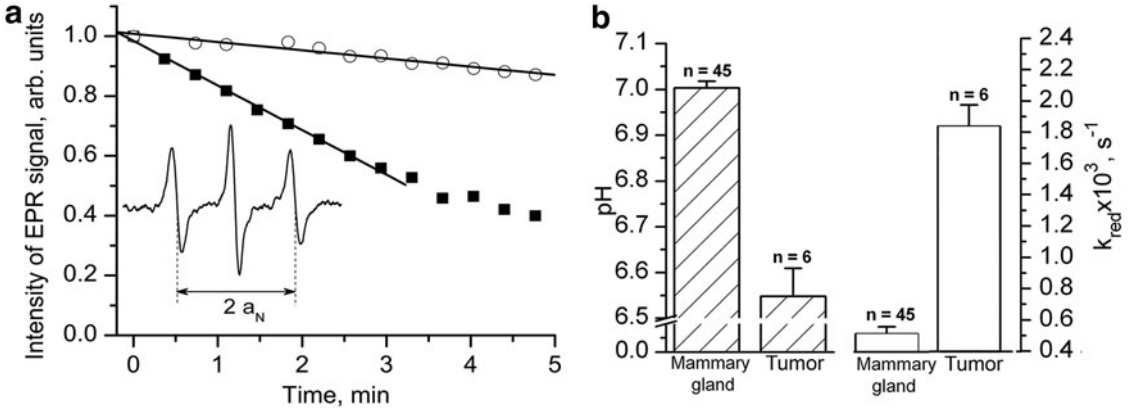

FIG. 6. ***In vivo*** **pH and redox assessment of TME in mouse model of breast cancer using dual-function NR1 probe.** **(a)** EPR *insert:* L-band EPR spectrum of the NR1 probe measured after i.t. injection (10 μL, 10 m*M*) in mammary tumor tissue of anesthetized female FVB/N mice. The hyperfine splitting, a_N, was found to be equal to 14.72 G, which corresponds to the value of $pH_e = 6.52$ assuming tumor tissue temperature 34°C and $pK_a = 6.65$. NR1 reduction rate is assessed by the following: the decay of central-field spectral component. The exemplified kinetics measured in mammary tumor (■) and mammary glands (○) demonstrates a higher reducing capacity of the tumor tissue *versus* normal mammary gland. The analysis of the initial part of the kinetics yields the rates of the EPR signal reduction, k_{red}, in extracellular media of the tissues being equal to 2.5×10^{-3} s^{-1} in tumor *versus* 0.5×10^{-3} s^{-1} in normal gland. **(b)** Extracellular tissue pH (*filled bars*) and the reduction rate (*empty bars*) values of NR1 nitroxide in normal mammary glands and mammary tumors of female FVB/N mice measured by *in vivo* EPR. Error bars denote SE. Adapted from Ref. (10) with permission.

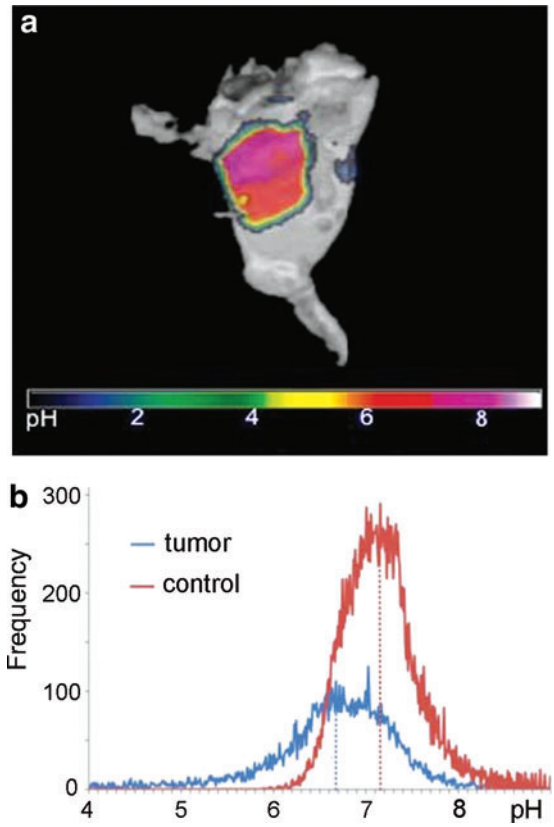

FIG. 7. Mapping of extracellular tumor pH. (a) Coregistered EPR pH map and MRI of right hind leg of C3H mouse bearing squamous cell carcinoma. A 4D (1×spectral, 3×spatial) 750 MHz continuous waves EPRI of low-field and high-field EPR peaks were performed using the following parameters: scan time, 0.3 s; modulation amplitude, 1.5 G; Gmax, 16 G/cm; FOV, 5.09 cm; projections, 576; and total acquisition time, ≈6 min. EPR pH map was superimposed with six Varian 7T MRI image. **(b)** pH distributions from 3D volume measurement of right hind leg from control and tumor-bearing mice. Adapted from Goodwin *et al.* (38) with permission. EPRI, EPR imaging. To see this illustration in color, the reader is referred to the web version of this article at www.liebertpub.com/ars

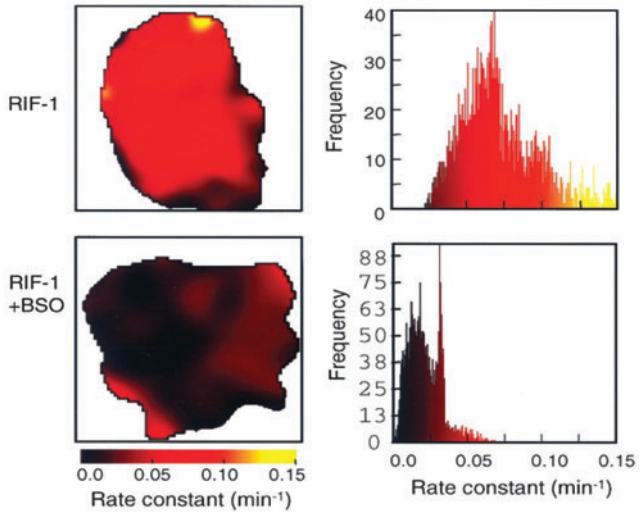

FIG. 8. Redox mapping of tumor. Two-dimensional spatial mapping of pseudofirst-order rate constants (*left panels*) and frequency plot (*right panels*) of the nitroxide reduction rate constants in the TME of untreated and BSO-treated mice are shown. Reproduced from Ref. (70) with permission. To see this illustration in color, the reader is referred to the web version of this article at www.liebertpub.com/ars

Figures 7 and 8 illustrate the applications of EPRI for pH (38) and redox (70) mapping of the TME in living mice using nitroxide probes. The three-dimensional EPR map of extracellular pH in TME of squamous cell carcinoma in right hind leg of C3H mouse was measured after i.v. injection of cell-impermeable NR1 probe (Fig. 7a). Figure 7b shows a significantly more heterogeneous and acidic distribution of pH_e values in TME compared to normal tissue.

Figure 8 demonstrates the EPRI of TME reducing capacity measured in RIF-1 tumor-bearing mice using cell-permeable 3-carbamoyl-proxyl nitroxide probe (70). An observation of significant decrease in the rates of the NR signal decay for the mice treated with glutathione biosynthesis inhibitor, L-buthionine-*S,R*-sulfoximine, supports an important role of GSH as an intracellular redox buffer.

In vivo *EPR assessment of intracellular GSH*

A ubiquitous thiol-containing tripeptide, GSH, presents in virtually all mammalian tissues and plays a central role in cell biology. The intracellular GSH concentrations in mammalian cells are in the range between 1 and 10 m*M* and are close to half of the total thiols/disulfides in the cells. The redox couple of reduced GSH form and its oxidized disulfide form, GSSG, is a major component of intracellular redox buffer (92, 95). A metabolic reprogramming in proliferating cancer cells results in enhanced NADPH formation *via* the pentose phosphate pathway interconnected with glycolysis followed by facilitation of reduced GSH synthesis. High concentrations of GSH and low negative GSH redox potentials have been found in cancer cells of various tumor types (10, 33, 48, 103, 105). Furthermore, it has been demonstrated that tumor redox status can be modified by tissue glutathione level, *in vivo* (70). An increased level of GSH has been found in whole blood samples from patients with nonsmall-cell lung cancer (35) apparently reflecting high GSH concentration and low redox potential characteristic for proliferating malignant cells of distant malignant tissue.

The EPR approach allowing for assessment of glutathione redox status *in vivo* using GSH-sensitive probes might provide a useful indicator of cancer progression and aggressiveness. Currently, EPR spectroscopy, in combination with the disulfide biradicals of the imidazolidine type (59) (see Fig. 2 for the RSSR structure) and its isotopically substituted analogs (93), represents the only method that allows for noninvasive quantitative [GSH] measurements in living subjects in preclinical applications (10, 93). The RSSR probe represents a paramagnetic analog of disulfide Ellman's reagent (24, 25), which on the reaction of thiol/disulfide exchange with GSH splits its disulfide bond resulting in formation of two monoradicals and cancelation of intramolecular spin-exchange between the monoradical fragments. Figure 9a illustrates the effect of reaction of the RSSR

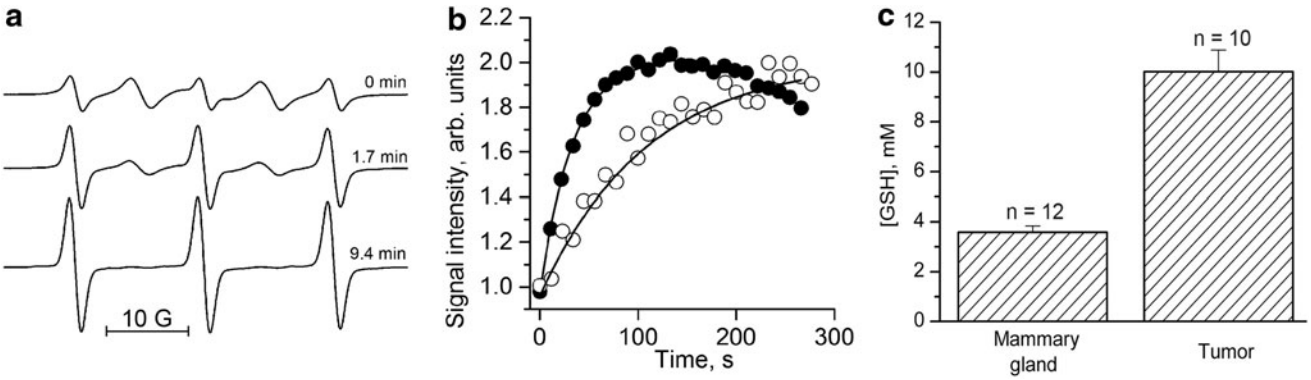

FIG. 9. EPR assessment of intracellular glutathione. (a) The X-band EPR spectra of 100 μM RSSR measured at various time points after incubation with 2.5 mM GSH in 0.1 M Na-phosphate buffer, pH 7.2, and 1 mM DTPA at 34°C. The kinetics analysis provides the observed rate constant value of the reaction between GSH and RSSR, k_{obs}(pH 7.2, 34°C) = (2.8 ± 0.2) M^{-1} s^{-1}. **(b)** Kinetics of the monoradical spectral peak intensity change measured by L-band EPR in mammary tumor (●) and normal mammary gland (○) of FVB/N mice immediately after i.t. injection of RSSR probe. The *solid lines* are the fits of the initial part of the kinetics by the monoexponent supposing k_{obs} (pH 7.2, 34°C) = 2.8 $M^{-1}s^{-1}$ and yielding [GSH] = 10.7 and 3.3 mM for the tumor and normal mammary gland, correspondingly. (**c**) Intracellular [GSH] measured using R_2SSR_2 probe *in vivo* in normal mammary glands and mammary tumors of female FVB/N mice. Adapted from Ref. (10) with permission from John Wiley & Sons, Inc.

probe with glutathione on the EPR spectra resulting in disappearance of the ''biradical'' spectral components and a corresponding increase of the intensity of the monoradical components. The rate of the increase of the amplitude of the monoradical component is proportional to the GSH concentration and is a convenient GSH-sensitive EPR spectral parameter. The observed rate constant of the reaction between GSH and RSSR, $k_{obs} = 2.8 \pm 0.2$ $M^{-1}s^{-1}$ (T = 34°C, pH 7.2) (10). This corresponds to the time constants of exponential kinetics in the range from 0.6 to 6 min for the physiologically relevant intracellular GSH concentration from 1 to 10 mM providing an experimentally convenient time window for the EPR detection. Note that the RSSR disulfide biradical being a small lipophilic molecule easily crosses cellular membranes where it reacts with intracellular GSH providing a reliable approach for determination of GSH, *in vivo* (10, 93). This EPR approach relies on a major contribution of the intracellular glutathione in the pool of the thiols easily accessible for the reaction with the disulfide biradicals. Figure 9b exemplifies the kinetics of the monoradical spectral peak intensity change measured in mammary tumor (●) and normal mammary gland (○) using L-band EPR. The solid lines are the fits of the initial part of the kinetics by the monoexponent yielding [GSH] = 10.7 and 3.3 mM for the tumor and normal mammary gland, correspondingly.

Recently, new disulfide paramagnetic reagents, including disulfide biradicals of pyrrolidine type (73), trityl-nitroxide and trityl-trityl disulfide biradicals (78), were synthesized. Trityl disulfides are cell impermeable (78) and do not allow assessment of intracellular GSH. The use of pyrrolidine disulfides for EPR assessment of thiols was demonstrated *in vitro* (22, 73) and then *in vivo* for mapping thiol redox status in tumor-bearing mice (31). Further comparative studies of the rates of the penetration of the pyrrolidine disulfide nitroxides into the cells, their reaction with GSH, and reduction by intracellular reductants are required to determine the capacity of these probes for quantitative *in vivo* EPR measurement of intracellular glutathione concentrations.

In vivo *concurrent EPR measurements of tissue* pO_2, pH_e, *and Pi*

Concurrent *in vivo* EPR measurements of the multiple TME parameters using a single paramagnetic probe allow for their correlation analysis independent of probe distribution, time of probe delivery, and spectrum acquisition, therefore providing unique insight into the relationships between these parameters in solid tumors (45). Recently, we designed a trityl paramagnetic probe, HOP*E*, with unique spectral properties (8, 20) that allowed for simultaneous *in vivo* monitoring of tissue pH, pO_2, and [Pi] in extracellular microenvironment in various animal models of cancer (9, 20). Note that ^{31}P NMR of endogenous phosphate predominantly measures intracellular phosphate while EPR detects the HOP*E* probe in interstitial extracellular space: bulky hydrophilic HOP*E* probe does not cross cellular membrane and its EPR signal from the blood is not observed due to probe complexation with plasma albumin (96). Figure 10 illustrates functional sensitivities of the spectral parameters of the HOP*E* probe.

Figure 11 illustrates multifunctional measurements performed in FVB/N wild-type mammary glands and in the TME of MMTV-PyMT transgenic mice, which spontaneously develop breast cancer and emulate human tumor staging (74). The comparison of the mean values of pO_2 in tumors and in normal tissues (50 ± 3 mmHg *vs.* 58 ± 3 mmHg, correspondingly) and pH_e (6.99 ± 0.03 in TME *vs.* 7.1 ± 0.03 in normal tissue) supports an appearance of hypoxic and acidic regions in the tumor. The most significant several-fold differences were observed for interstitial [Pi] (1.8 ± 0.2 mM in TME *vs.* 0.84 ± 0.07 mM in normal tissue), indicating a potential role of interstitial Pi as TME marker of tumor progression. Figure 11e–h shows the correlation between the individual values of the TME parameters measured with the HOP*E* probe. The observed positive correlation between pO_2 and pH_e in normal tissue *versus* the absence of correlation between these parameters in tumors supports tumor

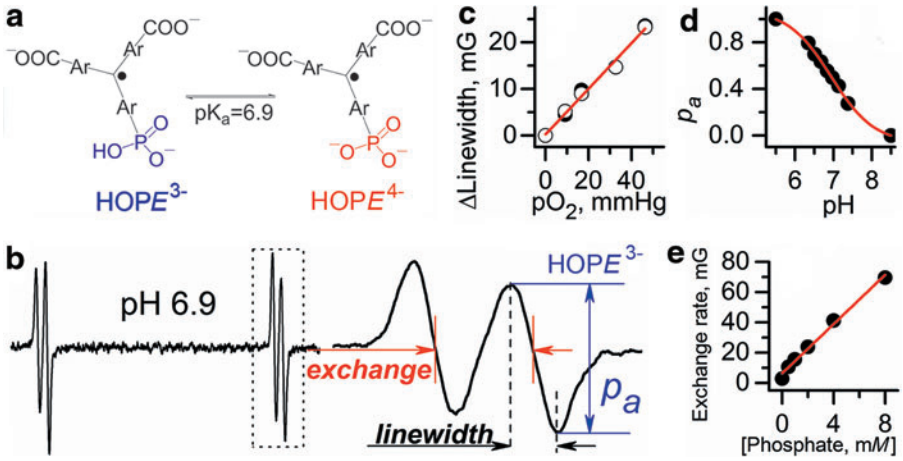

FIG. 10. Multifunctional assessment of chemical microenvironment using HOP*E* probe. **(a)** The scheme of pH-dependent equilibrium between two ionization states of the probe. **(b)** L-band EPR spectrum of HOP*E*. **(c)** The EPR linewidth of the HOP*E* is a pO_2 marker (accuracy, $\approx$1 mmHg; pO_2 range, 1–100 mmHg). **(d)** The fraction of HOPE^{3-} form is a pH marker in the range from 6 to 8.0 (accuracy, ±0.05). **(e)** Dependence of proton exchange rate (expressed in mG) of the HOP*E* with inorganic phosphate on Pi concentration extracted by spectra simulation (accuracy, ±0.1 mM, range, 0.1–20 mM) (8, 20). Reproduced from ref. (9) with permission from Nature Publishing Group. To see this illustration in color, the reader is referred to the web version of this article at www.liebertpub.com/ars

reliance on glycolytic metabolism independent of oxygen availability—the latter exemplifies *in vivo* manifestation of Warburg effect. Figure 11g and h shows negative correlation between pO_2 and [Pi] both in normal tissue and TME supporting association of increase in [Pi] with changes in bioenergetic status on insufficient oxygen delivery.

The EPR profiling of TME of nonmetastatic PC14 and metastatic PC14HM tumor xenografts using HOP*E* probe showed that pO_2 and pH_e values do not significantly differ for these two xenografts (9). On the contrary, extracellular inorganic phosphate concentrations allowed for discriminating between nonmetastatic and metastatic tumors—the measured

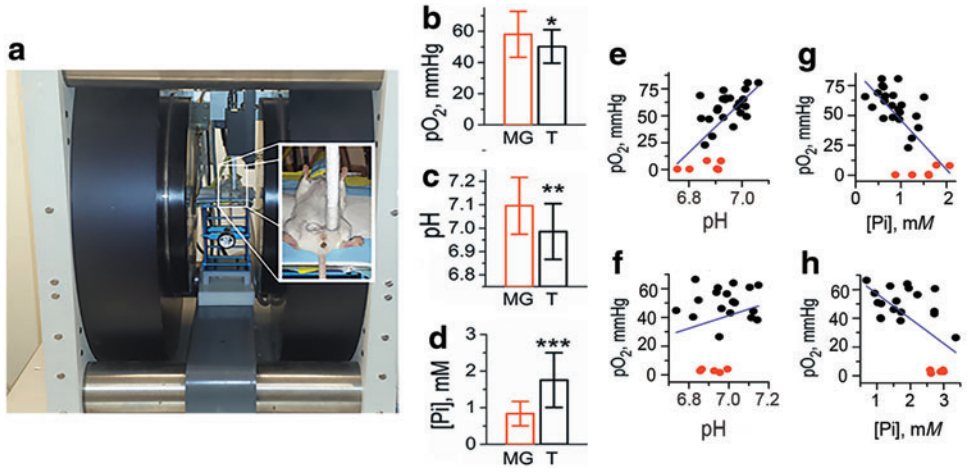

FIG. 11. (a) Setup for *in vivo* L-band EPR measurements of the tissue microenvironment parameters in living mice. Photograph shows the anesthetized mouse between the magnets of the EPR spectrometer with the insert on the *right* showing placement and positioning of the loop resonator on *top* of the measured tissue. The values of pO_2 **(b)**, pH_e **(c)**, and [Pi] **(d)** measured in normal mammary glands of FVB/N wild-type mice (MG, $n=23$) and in the TME of breast cancer in MMTV-PyMT transgenic mice (T, $n=18$). Error bars are SD.*$p=0.065$, **$p=0.006$, ***$p=6\times10^{-6}$. **(e–h)** Correlation between interstitial pO_2, pH_e, and Pi values measured in MG and in the TME. To extend the range of oxygen variations, anoxic conditions in interstitial space were established by i.t. injection of oxygen-consuming enzymatic system of glucose/glucose oxidase (*red* symbols). *Blue lines* represent linear fit for the total data sets. **(e)** A positive correlation between pO_2 and pH_e in normal tissue ($r=0.5$, $p=0.014$ for *black* symbols; $r=0.64$, $p=1.8\times10^{-4}$ for total data set) *versus* **(f)** no significant correlation between pO_2 and pH_e in TME ($r=0.01$, $p=0.97$ for *black* symbols; $r=0.23$, $p=0.3$ for total data set) was found. **(g)** A negative correlation between pO_2 and Pi both in normal tissue ($r=-0.51$, $p=0.013$ for *black* symbols; $r=-0.7$, $p=2.3\times10^{-5}$ for total data set) and **(h)** in TME (b, *bottom*: $r=-0.4$, $p=0.079$ for *black* symbols; $r=-0.62$, $p=0.001$ for total data set) was found. Adapted from Ref. (9) with permission. To see this illustration in color, the reader is referred to the web version of this article at www.liebertpub.com/ars

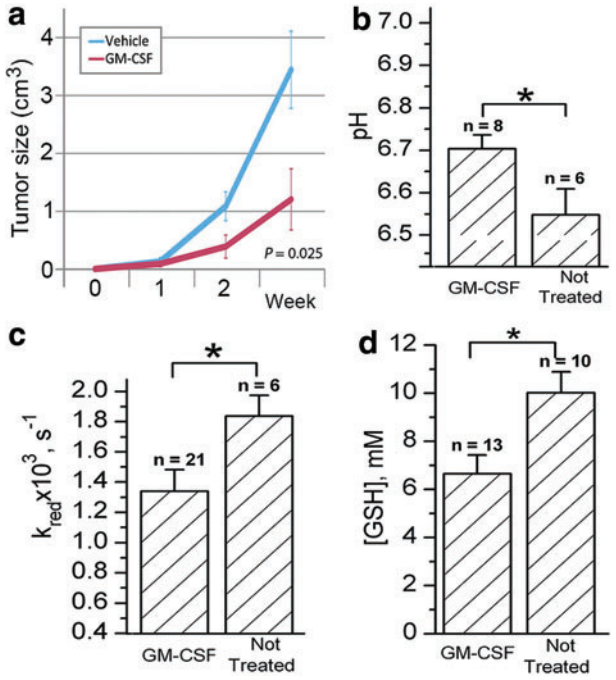

FIG. 12. Intratumor GM-CSF injection slows tumor growth and normalizes TME parameters. (a) PyMT+ FVB female mice with palpable tumors were treated with PBS or 100 ng GM-CSF by intratumor injection thrice per week. Points, mean tumor size from 8 (GM-CSF) and 10 (PBS) mice; bars, SE. Adapted from Ref. (34) with permission. **(b–d)** Normalization of TME of GM-CSF-treated tumors as measured by *in vivo* EPR (measurements started 1 week after treatment initiation). The values of pH **(b)** and reducing capacity of extracellular TME **(c)** were measured using NR1 probe, and intracellular GSH values were measured using RSSR probe **(d)**. Error bars denote SE. Adapted from Ref. (10) with permission. GM-CSF, granulocyte macrophage colony-stimulating factor; PBS, phosphate-buffered saline. To see this illustration in color, the reader is referred to the web version of this article at www.liebertpub.com/ars

levels of [Pi] were significantly higher in the metastatic PC14HM xenografts (9). The associate of high interstitial Pi concentrations with alterations in tumor metabolism (98, 102), Pi contribution in buffer-facilitated proton transport (39), and a high demand in phosphorus supply for the rapid growth according to the ''growth rate hypothesis'' (26) may underline the potential contribution in tumor progression and aggressiveness [see Ref. (9) for detailed discussion]. Further studies are required to evaluate physiological significance of the observed high TME phosphate concentrations and the amplification in highly metastatic tumors, and whether it may provide additional opportunities for TME-targeted therapy.

Janus-faced TME and EPR profiling of normalization during anticancer treatment

The increased rates of ROS generation (5, 75, 80, 87) and lipid peroxidation (32, 72) have been measured in many cancers. We hypothesized (55) that specific TME parameters deviate from the corresponding counterparts in normal tissues facilitating extracellular ROS production and exposing cancer and nontransformed cells to a highly oxidizing environment. The cancer cells are well equipped with overexpressed antioxidant defense to survive in oxidative TME. On the other side, an exposure of the normal cells to a highly oxidizing environment may result in unavoidable and fatal toxicity. This ''Janus-faced'' character of the TME facilitates cancer growth at the expense of normal cells. Normalizing parameters of the tissue microenvironment may decrease selection pressure for malignant phenotype. Therefore, EPR monitoring of TME parameters during anticancer treatment may provide a tool for optimization of therapy efficiency and contribute to the development of TME-targeted therapeutic approaches.

Figure 12 illustrates an example of *in vivo* EPR profiling of TME using functional probes, NR1 and RSSR, during the treatment with anticancer drug (10). It has been reported a significant decrease in tumor growth (Fig. 12a), angiogenesis, metastases, and pO_2 level on treatment with granulocyte macrophage colony-stimulating factor (GM-CSF) in a PyMT model of breast cancer (34). Figure 12b–d shows EPR-measured TME parameters of PyMT mice bearing breast cancer tumors not treated and treated with GM-CSF. Note significant normalization of TME parameters on treatment with GM-CSF, namely, an increase of pH_e, decrease of tissue reducing capacity, and GSH concentration.

Conclusions

The recent progress in EPR instrumentation designed to be used in humans (100) and the development of biocompatible paramagnetic probes with spectral sensitivity to the parameters of local chemical microenvironment eventually will make possible the translation of EPR techniques for multifunctional profiling of TME into clinical settings. These techniques will allow improving prediction power of early diagnostics for malignant transition and for future rational design of TME-targeted anticancer therapeutics.

Acknowledgments

This work was partially supported by NIH grants CA194013, CA192064, and U54GM104942. The WVCTSI is acknowledged for start-up to V.V.K. The content is solely the responsibility of the author and does not necessarily represent the official views of the NIH.

Author Disclosure Statement

No competing financial interests exist.

References

1. Ardenkjaer-Larsen JH, Laursen I, Leunbach I, Ehnholm G, Wistrand LG, Petersson JS, and Golman K. EPR and DNP properties of certain novel single electron contrast agents intended for oximetric imaging. *J Magn Reson* 133: 1–12, 1998.
2. Bacic G, Nilges MJ, Magin RL, Walczak T, and Swartz HM. In vivo localized ESR spectroscopy reflecting metabolism. *Magn Reson Med* 10: 266–272, 1989.
3. Backer JM, Budker VG, Eremenko SI, and Molin YN. Detection of the kinetics of biochemical reactions with oxygen using exchange broadening in the ESR spectra of

nitroxide radicals. *Biochim Biophys Acta* 460: 152–156, 1977.
4. Barriga-Gonzalez G, Olea-Azar C, Zuniga-Lopez MC, Folch-Cano C, Aguilera-Venegas B, Porcal W, Gonzalez M, and Cerecetto H. Spin trapping: An essential tool for the study of diseases caused by oxidative stress. *Curr Top Med Chem* 15: 484–495, 2015.
5. Bauer G. Tumor cell-protective catalase as a novel target for rational therapeutic approaches based on specific intercellular ROS signaling. *Anticancer Res* 32: 2599–2624, 2012.
6. Bobko AA, Dhimitruka I, Eubank TD, Marsh CB, Zweier JL, and Khramtsov VV. Trityl-based EPR probe with enhanced sensitivity to oxygen. *Free Radic Biol Med* 47: 654–658, 2009.
7. Bobko AA, Dhimitruka I, Zweier JL, and Khramtsov VV. Trityl radicals as persistent dual function pH and oxygen probes for in vivo electron paramagnetic resonance spectroscopy and imaging: concept and experiment. *J Am Chem Soc* 129: 7240–7241, 2007.
8. Bobko AA, Dhimitruka I, Zweier JL, and Khramtsov VV. Fourier transform EPR of trityl radicals for multifunctional assessment of chemical microenvironment. *Angew Chem Int Edit* 53: 2735–2738, 2014.
9. Bobko AA, Eubank TD, Driesschaert B, Dhimitruka I, Evans J, Mohammad R, Tchekneva EE, Dikov MM, and Khramtsov VV. Interstitial inorganic phosphate as a tumor microenvironment marker for tumor progression. *Sci Rep* 7: 41233, 2017.
10. Bobko AA, Eubank TD, Voorhees JL, Efimova OV, Kirilyuk IA, Petryakov S, Trofimiov DG, Marsh CB, Zweier JL, Grigor'ev IA, Samouilov A, and Khramtsov VV. In vivo monitoring of pH, redox status, and glutathione using L-band EPR for assessment of therapeutic effectiveness in solid tumors. *Magn Reson Med* 67: 1827–1836, 2012.
11. Bobko AA, Evans J, Denko NC, and Khramtsov VV. Concurrent longitudinal EPR monitoring of tissue oxygenation, acidosis, and reducing capacity in mouse xenograft tumor models. *Cell Biochem Biophys* 75: 247–253, 2017.
12. Brahimi-Horn MC, Chiche J, and Pouyssegur J. Hypoxia signalling controls metabolic demand. *Curr Opin Cell Biol* 19: 223–229, 2007.
13. Bratasz A, Selvendiran K, Wasowicz T, Bobko A, Khramtsov VV, Ignarro LJ, and Kuppusamy P. NCX-4040, a nitric oxide-releasing aspirin, sensitizes drug-resistant human ovarian xenograft tumors to cisplatin by depletion of cellular thiols. *J Transl Med* 6: 9, 2008.
14. Camalier CE, Yi M, Yu LR, Hood BL, Conrads KA, Lee YJ, Lin Y, Garneys LM, Bouloux GF, Young MR, Veenstra TD, Stephens RM, Colburn NH, Conrads TP, and Beck GR, Jr. An integrated understanding of the physiological response to elevated extracellular phosphate. *J Cell Physiol* 228: 1536–1550, 2013.
15. Camalier CE, Young MR, Bobe G, Perella CM, Colburn NH, and Beck GR, Jr. Elevated phosphate activates N-ras and promotes cell transformation and skin tumorigenesis. *Cancer Prev Res (Phila)* 3: 359–370, 2010.
16. Chang SH, Yu KN, Lee YS, An GH, Beck GR, Jr., Colburn NH, Lee KH, and Cho MH. Elevated inorganic phosphate stimulates Akt-ERK1/2-Mnk1 signaling in human lung cells. *Am J Respir Cell Mol Biol* 35: 528–539, 2006.
17. ClinicalTrials.gov. [Internet]. Bethesda, MD: National Library of Medicine (US). Identifier NCT02706197, Oxygen Measurements in Subcutaneous Tumors by EPR Oximetry Using OxyChip; 2016, March 11; Available at: https://clinicaltrials.gov/ct2/show/NCT02706197 (accessed December 11, 2017).
18. Cook JA, Gius D, Wink DA, Krishna MC, Russo A, and Mitchell JB. Oxidative stress, redox, and the tumor microenvironment. *Semin Radiat Oncol* 14: 259–266, 2004.
19. Dewhirst MW, Ong ET, Braun RD, Smith B, Klitzman B, Evans SM, and Wilson D. Quantification of longitudinal tissue pO(2) gradients in window chamber tumours: impact on tumour hypoxia. *Br J Cancer* 79: 1717–1722, 1999.
20. Dhimitruka I, Bobko AA, Eubank TD, Komarov DA, and Khramtsov VV. Phosphonated trityl probe for concurrent in vivo tissue oxygen and pH monitoring using EPR-based techniques. *J Am Chem Soc* 135: 5904–5910, 2013.
21. Dikalov SI, Polienko YF, and Kirilyuk IA. EPR measurements of reactive oxygen species by cyclic hydroxylamine spin probes. *Antioxid Redox Signal* 28: 1433–1443, 2018
22. Elajaili H, Biller JR, Rosen GM, Kao JP, Tseytlin M, Buchanan LA, Rinard GA, Quine RW, McPeak J, Shi Y, Eaton SS, and Eaton GR. Imaging disulfide dinitroxides at 250 MHz to monitor thiol redox status. *J Magn Reson* 260: 77–82, 2015.
23. Elas M, Williams BB, Parasca A, Mailer C, Pelizzari CA, Lewis MA, River JN, Karczmar GS, Barth ED, and Halpern HJ. Quantitative tumor oxymetric images from 4D electron paramagnetic resonance imaging (EPRI): Methodology and comparison with blood oxygen level-dependent (BOLD) MRI. *Magn Reson Med* 49: 682–691, 2003.
24. Ellman GL. A Colorimetric method for determining low concentrations of mercaptans. *Arch Biochem Biophys* 74: 443–450, 1958.
25. Ellman GL. Tissue sulfhydryl groups. *Arch Biochem Biophys* 82: 70–77, 1959.
26. Elser JJ, Kyle MM, Smith MS, and Nagy JD. Biological stoichiometry in human cancer. *PLoS One* 2: e1028, 2007.
27. Epel B and Halpern HJ. In vivo pO(2) imaging of tumors: Oxymetry with very low-frequency electron paramagnetic resonance. *Methods Enzymol* 564: 501–527, 2015.
28. Epel B, Kotecha M, and Halpern HJ. In vivo preclinical cancer and tissue engineering applications of absolute oxygen imaging using pulse EPR. *J Magn Reson* 280: 149–157, 2017.
29. Epel B, Krzykawska-Serda M, Tormyshev V, Maggio MC, Barth ED, Pelizzari CA, and Halpern HJ. Spin lattice relaxation EPR pO_2 images may direct the location of radiation tumor boosts to enhance tumor cure. *Cell Biochem Biophys* 75: 295–298, 2017.
30. Epel B, Redler G, Pelizzari C, Tormyshev VM, and Halpern HJ. Approaching oxygen-guided intensity-modulated radiation therapy. *Adv Exp Med Biol* 876: 185–193, 2016.
31. Epel B, Sundramoorthy SV, Krzykawska-Serda M, Maggio MC, Tseytlin M, Eaton GR, Eaton SS, Rosen GM, Kao JPY, and Halpern HJ. Imaging thiol redox status in murine tumors in vivo with rapid-scan electron paramagnetic resonance. *J Magn Reson* 276: 31–36, 2017.
32. Erejuwa OO, Sulaiman SA, and Ab Wahab MS. Evidence in support of potential applications of lipid peroxidation products in cancer treatment. *Oxid Med Cell Longev* 2013: 931251, 2013.

33. Estrela JM, Ortega A, and Obrador E. Glutathione in cancer biology and therapy. *Crit Rev Clin Lab Sci* 43: 143–181, 2006.
34. Eubank TD, Roberts RD, Khan M, Curry JM, Nuovo GJ, Kuppusamy P, and Marsh CB. Granulocyte macrophage colony-stimulating factor inhibits breast cancer growth and metastasis by invoking an anti-angiogenic program in tumor-educated macrophages. *Cancer Res* 69: 2133–2140, 2009.
35. Ferruzzi E, Franceschini R, Cazzolato G, Geroni C, Fowst C, Pastorino U, Tradati N, Tursi J, Dittadi R, and Gion M. Blood glutathione as a surrogate marker of cancer tissue glutathione S-transferase activity in non-small cell lung cancer and squamous cell carcinoma of the head and neck. *Eur J Cancer* 39: 1019–1029, 2003.
36. Gade TP, Buchanan IM, Motley MW, Mazaheri Y, Spees WM, and Koutcher JA. Imaging intratumoral convection: Pressure-dependent enhancement in chemotherapeutic delivery to solid tumors. *Clin Cancer Res* 15: 247–255, 2009.
37. Gillies RJ, Raghunand N, Garcia-Martin ML, and Gatenby RA. pH imaging. A review of pH measurement methods and applications in cancers. *IEEE Eng Med Biol Mag* 23: 57–64, 2004.
38. Goodwin J, Koda S, Ohfuchi M, Pawlak A, Yasui H, Khramstov V, and Hirata H. Four-dimensional spectral spatial pH mapping of mouse tumour using Continuous Wave-Electron Paramagnetic Resonance imaging (CW-EPRI) and pH sensitive imidazoline nitroxide. In: *Proceedings of the 20th Annual Meeting of the International Society for Magnetic Resonance in Medicine*. Melbourne, Australia, 2012, p. 1708. http://cds.ismrm.org/protected/12MProceedings/files/1708.pdf
39. Griffith JR, McIntyre DJ, Howe FA, and Stubbs M. Why are cancers acidic? A carrier-mediated diffusion model for H^+ transport in the inerstitial fluid. *Novartis Foundation Symp* 240: 46–62, 2001.
40. Guiberteau T and Grucker D. Dynamic nuclear polarization imaging in very low magnetic fields as a noninvasive technique for oximetry. *J Magn Reson* 124: 263–266, 1997.
41. Halpern HJ, Yu C, Peric M, Barth E, Grdina DJ, and Teicher BA. Oxymetry deep in tissues with low-frequency electron-paramagnetic-resonance. *Proc Natl Acad Sci U S A* 91: 13047–13051, 1994.
42. This reference has been deleted.
43. Hardy M, Zielonka J, Karoui H, Sikora A, Michalski R, Podsiadły R, Lopez M, Vasquez-Vivar J, Kalyanaraman B, and Ouari O. Detection and characterization of reactive oxygen and nitrogen species in biological systems by monitoring species-specific products. *Antioxid Redox Signal* 28: 1416–1432, 2018.
44. Haulica A and Ababei L. Comparative study of glycolytic activity in the erythrocytes of animals with chronic experimental hypoxia and with tumours. *Neoplasma* 21: 29–35, 1974.
45. Helmlinger G, Yuan F, Dellian M, and Jain RK. Interstitial pH and pO(2) gradients in solid tumors in vivo: high-resolution measurements reveal a lack of correlation. *Nat Med* 3: 177–182, 1997.
46. Hockel M, Schlenger K, Aral B, Mitze M, Schaffer U, and Vaupel P. Association between tumor hypoxia and malignant progression in advanced cancer of the uterine cervix. *Cancer Res* 56: 4509–4515, 1996.
47. Hockel M and Vaupel P. Tumor hypoxia: definitions and current clinical, biologic, and molecular aspects. *J Natl Cancer Inst* 93: 266–276, 2001.
48. Huang Z, Komninou D, Kleinman W, Pinto JT, Gilhooly EM, Calcagnotto A, and Richie JP, Jr. Enhanced levels of glutathione and protein glutathiolation in rat tongue epithelium during 4-NQO-induced carcinogenesis. *Int J Cancer* 120: 1396–1401, 2007.
49. Hyde JS, Jin J-J, Felix JB, and Hubbell WL. Advances in spin label oximetry. *Pure Appl Chem* 62: 255–260, 1990.
50. Hyodo F, Matsumoto S, Devasahayam N, Dharmaraj C, Subramanian S, Mitchell JB, and Krishna MC. Pulsed EPR imaging of nitroxides in mice. *J Magn Reson* 197: 181–185, 2009.
51. Jin H, Xu CX, Lim HT, Park SJ, Shin JY, Chung YS, Park SC, Chang SH, Youn HJ, Lee KH, Lee YS, Ha YC, Chae CH, Beck GR, Jr., and Cho MH. High dietary inorganic phosphate increases lung tumorigenesis and alters Akt signaling. *Am J Respir Crit Care Med* 179: 59–68, 2009.
52. Khoshniat S, Bourgine A, Julien M, Weiss P, Guicheux J, and Beck L. The emergence of phosphate as a specific signaling molecule in bone and other cell types in mammals. *Cell Mol Life Sci* 68: 205–218, 2011.
53. Khramtsov VV. Biological imaging and spectroscopy of pH. *Curr Org Chem* 9: 909–923, 2005.
54. Khramtsov VV. In vivo spectroscopy and imaging of nitroxide probes. In: *Nitroxides—Theory, Experiment and Applications,* edited by Kokorin AI. Rijeka, Croatia: InTech, 2012, pp. 317–346.
55. Khramtsov VV and Gillies RJ. Janus-faced tumor microenvironment and redox. *Antioxid Redox Signal* 21: 723–729, 2014.
56. Khramtsov VV, Grigor'ev IA, Foster MA, Lurie DJ, and Nicholson I. Biological applications of spin pH probes. *Cell Mol Biol* 46: 1361–1374, 2000.
57. Khramtsov VV, Grigor'ev IA, Foster MA, Lurie DJ, Zweier JL, and Kuppusamy P. Spin pH and SH probes: Enhancing functionality of EPR-based techniques. *Spectroscopy* 18: 213–225, 2004.
58. Khramtsov VV, Weiner LM, Grigor'ev IA, and Volodarsky LB. Proton exchange in stable nitroxyl radicals. EPR studies of the pH of aqueous solutions. *Chem Phys Lett* 91: 69–72, 1982.
59. Khramtsov VV, Yelinova VI, Glazachev Yu I, Reznikov VA, and Zimmer G. Quantitative determination and reversible modification of thiols using imidazolidine biradical disulfide label. *J Biochem Biophys Methods* 35: 115–128, 1997.
60. Kirilyuk IA, Bobko AA, Grigor'ev IA, and Khramtsov VV. Synthesis of the tetraethyl substituted pH-sensitive nitroxides of imidazole series with enhanced stability towards reduction. *Org Biomol Chem* 2: 1025–1030, 2004.
61. Kishimoto S, Krishna MC, Khramtsov VV, Utsumi H, and Lurie DJ. In vivo application of proton electron double resonance imaging. *Antioxid Redox Signal* 28: 1345–1364, 2018.
62. Kishimoto S, Matsumoto K, Saito K, Enomoto A, Matsumoto S, Mitchell JB, Nallathamby D, and Krishna MC. Pulsed EPR imaging: Applications in the studies of tumor physiology. *Antioxid Redox Signal* 28: 1378–1393, 2018.
63. Kocherginsky N and Swartz HM. *Nitroxide Spin Labels. Reactions in Biology and Chemistry* Boca Raton, New York, London, Tokyo: CRC Press, 1995, p. 270.

64. Komarov DA, Dhimitruka I, Kirilyuk IA, Trofimiov DG, Grigor'ev IA, Zweier JL, and Khramtsov VV. Electron paramagnetic resonance monitoring of ischemia-induced myocardial oxygen depletion and acidosis in isolated rat hearts using soluble paramagnetic probes. *Magn Reson Med* 68: 649–655, 2012.
65. Kosem N, Naganuma T, Ichikawa K, Morales NP, Yasukawa K, Hyodo F, Yamada K, and Utsumi H. Whole-body kinetic image of a redox probe in mice using Overhauser-enhanced MRI. *Free Radic Biol Med* 53: 328–336, 2012.
66. Krishna MC, English S, Yamada K, Yoo J, Murugesan R, Devasahayam N, Cook JA, Golman K, Ardenkjaer-Larsen JH, Subramanian S, and Mitchell JB. Overhauser enhanced magnetic resonance imaging for tumor oximetry: Coregistration of tumor anatomy and tissue oxygen concentration. *Proc Natl Acad Sci U S A* 99: 2216–2221, 2002.
67. Kubota H, Komarov DA, Yasui HB, Matsumoto S, Inanami O, Kirilyuk IA, Khramtsov VV, and Hirata HS. Feasibility of in vivo three-dimensional T-2(*) mapping using dicarboxy-PROXYL and CW-EPR-based single-point imaging. *Magn Reson Mater Phys Biol Med* 30: 291–298, 2017.
68. Kuppusamy P, Afeworki M, Shankar RA, Coffin D, Krishna MC, Hahn SM, Mitchell JB, and Zweier JL. In vivo electron paramagnetic resonance imaging of tumor heterogeneity and oxygenation in a murine model. *Cancer Res* 58: 1562–1568, 1998.
69. Kuppusamy P and Krishna MC. EPR imaging of tissue redox status. *Curr Top Biophys* 26: 29–34, 2002.
70. Kuppusamy P, Li H, Ilangovan G, Cardounel AJ, Zweier JL, Yamada K, Krishna MC, and Mitchell JB. Noninvasive imaging of tumor redox status and its modification by tissue glutathione levels. *Cancer Res* 62: 307–312, 2002.
71. Lai CS, Hopwood LE, Hyde JS, and Lukiewicz S. ESR studies of O2 uptake by Chinese hamster ovary cells during the cell cycle. *Proc Natl Acad Sci U S A* 79: 1166–1170, 1982.
72. Lauschke H, Tolba R, Burger B, Minor T, and Hirner A. Lipid peroxidation as additional marker in patients with colorectal cancer. Results of a preliminary study. *Eur Surg Res* 34: 346–350, 2002.
73. Legenzov EA, Sims SJ, Dirda NDA, Rosen GM, and Kao JPY. Disulfide-linked dinitroxides for monitoring cellular thiol redox status through electron paramagnetic resonance spectroscopy. *Biochemistry* 54: 6973–6982, 2015.
74. Lin EY, Jones JG, Li P, Zhu L, Whitney KD, Muller WJ, and Pollard JW. Progression to malignancy in the polyoma middle T oncoprotein mouse breast cancer model provides a reliable model for human diseases. *Am J Pathol* 163: 2113–2126, 2003.
75. Liou GY and Storz P. Reactive oxygen species in cancer. *Free Radic Res* 44: 479–496, 2010.
76. Liu KJ, Gast P, Moussavi M, Norby SW, Vahidi N, Walczak T, Wu M, and Swartz HM. Lithium phthalocyanine—A probe for electron-paramagnetic-resonance oximetry in viable biological-systems. *Proc Natl Acad Sci U S A* 90: 5438–5442, 1993.
77. This reference has been deleted
78. Liu YP, Song YG, Rockenbauer A, Sun J, Hemann C, Villamena FA, and Zweier JL. Synthesis of trityl radical-conjugated disulfide biradicals for measurement of thiol concentration. *J Org Chem* 76: 3853–3860, 2011.
79. Lora-Michiels M, Yu D, Sanders L, Poulson JM, Azuma C, Case B, Vujaskovic Z, Thrall DE, Charles HC, and Dewhirst MW. Extracellular pH and P-31 magnetic resonance spectroscopic variables are related to outcome in canine soft tissue sarcomas treated with thermoradiotherapy. *Clin Cancer Res* 12: 5733–5740, 2006.
80. Luanpitpong S, Talbott SJ, Rojanasakul Y, Nimmannit U, Pongrakhananon V, Wang L, and Chanvorachote P. Regulation of lung cancer cell migration and invasion by reactive oxygen species and caveolin-1. *J Biol Chem* 285: 38832–38840, 2010.
81. Matsumoto K, Hyodo F, Matsumoto A, Koretsky AP, Sowers AL, Mitchell JB, and Krishna MC. High-resolution mapping of tumor redox status by magnetic resonance imaging using nitroxides as redox-sensitive contrast agents. *Clin Cancer Res* 12: 2455–2462, 2006.
82. Matsumoto K, Subramanian S, Devasahayam N, Aravalluvan T, Murugesan R, Cook JA, Mitchell JB, and Krishna MC. Electron paramagnetic resonance imaging of tumor hypoxia: enhanced spatial and temporal resolution for in vivo pO(2) determination. *Magn Reson Med* 55: 1157–1163, 2006.
83. Maxwell PH, Dachs GU, Gleadle JM, Nicholls LG, Harris AL, Stratford IJ, Hankinson O, Pugh CW, and Ratcliffe PJ. Hypoxia-inducible factor-1 modulates gene expression in solid tumors and influences both angiogenesis and tumor growth. *Proc Natl Acad Sci U S A* 94: 8104–8109, 1997.
84. Meenakshisundaram G, Eteshola E, Pandian RP, Bratasz A, Lee SC, and Kuppusamy P. Fabrication and physical evaluation of a polymer-encapsulated paramagnetic probe for biomedical oximetry. *Biomed Microdevices* 11: 773–782, 2009.
85. Meenakshisundaram G, Pandian RP, Eteshola E, Lee SC, and Kuppusamy P. A paramagnetic implant containing lithium naphthalocyanine microcrystals for high-resolution biological oximetry. *J Magn Reson* 203: 185–189, 2010.
86. Molin YN, Salikhov KM, and Zamaraev KI. *Spin Exchange: Principles and Applications in Chemistry and Biology*. New York: Springer-Verlag, 1980, p. 242.
87. Oberley LW, Oberley TD, and Buettner GR. Cell division in normal and transformed cells: The possible role of superoxide and hydrogen peroxide. *Med Hypotheses* 7: 21–42, 1981.
88. Ojha N, Roy S, He G, Biswas S, Velayutham M, Khanna S, Kuppusamy P, Zweier JL, and Sen CK. Assessment of wound-site redox environment and the significance of Rac2 in cutaneous healing. *Free Radic Biol Med* 44: 682–691, 2008.
89. Pandian RP, Chacko SM, Kuppusamy ML, Rivera BK, and Kuppusamy P. Evaluation of Lithium Naphthalocyanine (LiNc) microcrystals for biological EPR oximetry. *Adv Exp Med Biol* 701: 29–36, 2011.
90. Pandian RP, Dolgos M, Marginean C, Woodward PM, Hammel PC, Manoharan PT, and Kuppusamy P. Molecular packing and magnetic properties of lithium naphthalocyanine crystals: Hollow channels enabling permeability and paramagnetic sensitivity to molecular oxygen. *J Mater Chem* 19: 4138–4147, 2009.
91. Pandian RP, Parinandi NL, Ilangovan G, Zweier JL, and Kuppusamy P. Novel particulate spin probe for targeted determination of oxygen in cells and tissues. *Free Radic Biol Med* 35: 1138–1148, 2003.
92. Pastore A, Federici G, Bertini E, and Piemonte F. Analysis of glutathione: Implication in redox and detoxification. *Clin Chim Acta* 333: 19–39, 2003.
93. Roshchupkina GI, Bobko AA, Bratasz A, Reznikov VA, Kuppusamy P, and Khramtsov VV. In vivo EPR measurement of glutathione in tumor-bearing mice using

improved disulfide biradical probe. *Free Rad Biol Med* 45: 312–320, 2008.
94. Samouilov A, Efimova OV, Bobko AA, Sun Z, Petryakov S, Eubank TD, Trofimov DG, Kirilyuk IA, Grigor'ev IA, Takahashi W, Zweier JL, and Khramtsov VV. In vivo proton-electron double-resonance imaging of extracellular tumor pH using an advanced nitroxide probe. *Analyt Chem* 86: 1045–1052, 2014.
95. Schafer FQ and Buettner GR. Redox environment of the cell as viewed through the redox state of the glutathione disulfide/glutathione couple. *Free Radic Biol Med* 30: 1191–1212, 2001.
96. Song YG, Liu YP, Liu WB, Villamena FA, and Zweier JL. Characterization of the binding of the Finland trityl radical with bovine serum albumin. *RSC Adv* 4: 47649–47656, 2014.
97. Spina A, Sapio L, Esposito A, Di Maiolo F, Sorvillo L, and Naviglio S. Inorganic phosphate as a novel signaling molecule with antiproliferative action in MDA-MB-231 breast cancer cells. *Biores Open Access* 2: 47–54, 2013.
98. Steen RG, Tamargo RJ, McGovern KA, Rajan SS, Brem H, Wehrle JP, and Glickson JD. In vivo 31P nuclear magnetic resonance spectroscopy of subcutaneous 9 L gliosarcoma: Effects of tumor growth and treatment with 1,3-bis(2-chloroethyl)-1-nitrosourea on tumor bioenergetics and histology. *Cancer Res* 48: 676–681, 1988.
99. Swartz HM, Liu KJ, Goda F, and Walczak T. India ink—A potential clinically applicable EPR Oximetry Probe. *Magn Reson Med* 31: 229–232, 1994.
100. Swartz HM, Williams BB, Zaki BI, Hartford AC, Jarvis LA, Chen EY, Comi RJ, Ernstoff MS, Hou H, Khan N, Swarts SG, Flood AB, and Kuppusamy P. Clinical EPR: Unique opportunities and some challenges. *Acad Radiol* 21: 197–206, 2014.
101. Tatum JL, Kelloff GJ, Gillies RJ, Arbeit JM, Brown JM, Chao KS, Chapman JD, Eckelman WC, Fyles AW, Giaccia AJ, Hill RP, Koch CJ, Krishna MC, Krohn KA, Lewis JS, Mason RP, Melillo G, Padhani AR, Powis G, Rajendran JG, Reba R, Robinson SP, Semenza GL, Swartz HM, Vaupel P, Yang D, Croft B, Hoffman J, Liu G, Stone H, and Sullivan D. Hypoxia: Importance in tumor biology, noninvasive measurement by imaging, and value of its measurement in the management of cancer therapy. *Int J Radiat Biol* 82: 699–757, 2006.
102. Tozer GM and Griffith JR. The contribution made by cell death and oxygenation to ^{31}P MRS observations of tumor energy metabolism. *NMR Biomed* 5: 279–289, 1992.
103. Traverso N, Ricciarelli R, Nitti M, Marengo B, Furfaro AL, Pronzato MA, Marinari UM, and Domenicotti C. Role of glutathione in cancer progression and chemoresistance. *Oxid Med Cell Longev* 2013: 972913, 2013.
104. Vaupel P, Kelleher DK, and Hockel M. Oxygenation status of malignant tumors: pathogenesis of hypoxia and significance for tumor therapy. *Semin Oncol* 28: 29–35, 2001.
105. Voegtlin C and Thompson JW. Glutathione content of tumor animals. *J Biol Chem* 70: 801–806, 1926.
106. Warburg O. On the origin of cancer cells. *Science* 123: 309–314, 1956.
107. Williams BB, Khan N, Zaki B, Hartford A, Ernstoff MS, and Swartz HM. Clinical electron paramagnetic resonance (EPR) oximetry using India ink. *Adv Exp Med Biol* 662: 149–156, 2010.
108. Woldman YY, Semenov SV, Bobko AA, Kirilyuk IA, Polienko JF, Voinov MA, Bagryanskaya EG, and Khramtsov VV. Design of liposome-based pH sensitive nanoSPIN probes: Nano-sized particles with incorporated nitroxides. *Analyst* 134: 904–910, 2009.

Address correspondence to:
Dr. Valery V. Khramtsov
In Vivo Multifunctional Magnetic Resonance center
Robert C. Byrd Health Sciences Center
West Virginia University
1 Medical Center Drive
Morgantown, WV 26506

E-mail: valery.khramtsov@hsc.wvu.edu

Date of first submission to ARS Central, August 22, 2017; date of final revised submission, October 13, 2017; date of acceptance, November 4, 2017.

Abbreviations Used

CW = continuous waves
EPR = electron paramagnetic resonance
EPRI = EPR imaging
GM-CSF = granulocyte macrophage colony-stimulating factor
GSH = glutathione
MRI = magnetic resonance imaging
Pi = phosphate
ROS = reactive oxygen species
TME = tumor microenvironment